

STAR CLUSTER FORMATION IN COSMOLOGICAL SIMULATIONS. I. YOUNG CLUSTER PROPERTIES

HUI LI^{1,*}, OLEG Y. GNEDIN¹, NICKOLAY Y. GNEDIN^{2,3,4}, XI MENG⁵, VADIM A. SEMENOV^{3,4}, ANDREY V. KRAVTSOV^{3,4,6}

(Dated: May 7, 2016)
 To be submitted to *ApJ*

ABSTRACT

We present a new star formation implementation, by considering star cluster as a unit of star formation and growing cluster particle continuously according to realistic cluster mass growth history. The mass growth of a given cluster particle is resolved in time and terminated by its own feedback, so that its final mass is obtained self-consistently. We investigate the properties of the model cluster particles in cosmological simulations of Milky Way-sized galaxies. We find that the cluster initial mass function (CIMF) is best described by a Schechter function. The power-law slope of CIMF is $\alpha \sim 1.8$ and the cutoff mass strongly depends on the star formation rate. We also find a positive correlation between the star formation rate surface density and fraction of clustered star formation. The formation of massive star clusters are preferred during starburst activities that are triggered by major merger events. We show that the mass growth history of cluster particles can be described by a decreasing mass growth rate, $\dot{M} \propto t^{-1/2}$, and the cluster formation timescale is as short as 4 Myr, consistent with the age spread of the observed young star clusters. The general agreement between the properties of the model star clusters and observations suggests that this implementation presents a reasonable way of modeling star formation in cosmological simulations and builds a bridge between star formation in small scales and galaxy formation in large scales.

Keywords: galaxies: formation — galaxies: star clusters — globular clusters: general

1. INTRODUCTION

One of the most important problems in astrophysics is understanding the formation and evolution of galaxies. Although the Λ cold dark matter paradigm shows a great success in reproducing observations on large scales and builds a solid theoretical framework (Planck Collaboration et al. 2014; Vikhlinin et al. 2009; Springel et al. 2006), many galaxy formation questions, especially the ones that involve with baryonic physics, are far from being answered. A self-consistent way of understanding the baryonic component of galaxies is to run simulations that include all relevant physics such as gravity, hydrodynamics, radiation, etc. This approach has already been proved to be a very important tool to study various aspects of galaxy formation. Current simulations are making rapid progress on reproducing different types of galaxies and observational empirical relations (such as the Kennicutt-Schmidt relation and global star formation history) by realizing the importance of stellar feedback on shaping the properties of the interstellar medium (e.g. Governato et al. 2012; Scannapieco et al. 2012; Hummels & Bryan 2012; Munshi et al. 2013; Hopkins et al. 2014; Agertz & Kravtsov 2015). These stellar feedback mechanisms suppress star formation activities at high red-shift and produce gas reservoir for star formation at lower red-shift.

Although various processes of stellar feedback have been

extensively explored (e.g. Katz 1992; Navarro & White 1993; Stinson et al. 2006; Scannapieco et al. 2006; Agertz et al. 2013; Ceverino et al. 2014; Salem & Bryan 2014; Keller et al. 2015), the star formation prescription has not changed for almost two decades since Katz (1992) and Cen & Ostriker (1992). In most of the current cosmological simulations, star particles are formed in cold and dense gas, with a rate that is calculated by assuming a fixed efficiency per free-fall time, ϵ_{ff} . Star particles are created by a Poisson process with their masses set beforehand.

Recent work including Agertz et al. (2013) and Agertz & Kravtsov (2015) found a strong impact of ϵ_{ff} on the galaxy star formation history, and illustrated a complex interplay between star formation and feedback. Semenov et al. (2015) explored the implementation of the turbulent-dependent ϵ_{ff} and found a wide range of local efficiency from 0.1 – 10%. These efforts suggest the importance of the sub-grid model of star formation on the general properties of simulated galaxies.

Young stars are usually found in a cluster environment (e.g. Lada & Lada 2003), and clusters can be considered as building blocks of the stellar component of galaxies. Thanks to the increasing computational power, current cosmological simulations have reached the regime that is able to resolve massive cluster formation regions with sufficient mass, spatial, and temporal resolutions (e.g. Hopkins et al. 2014; Read et al. 2015; Wetzel et al. 2016). Therefore, star formation implementation can be more realistic if the creation of star particle takes into account the processes of cluster formation in giant molecular clouds (GMCs). Moreover, observed properties of young massive star clusters, such as the cluster initial mass function (CIMF; e.g. Portegies Zwart et al. 2010) and the cluster formation timescale (Mac Low & Klessen 2004; Hartmann et al. 2012), can serve as tests for the star formation and feedback prescriptions on a scale that is comparable to the GMC.

In this paper, we develop a new model of implementing star formation by considering star cluster as a unit of star forma-

¹ Department of Astronomy, University of Michigan, Ann Arbor, MI 48109, USA

² Particle Astrophysics Center, Fermi National Accelerator Laboratory, Batavia, IL 60510, USA

³ Kavli Institute for Cosmological Physics, University of Chicago, Chicago, IL 60637, USA

⁴ Department of Astronomy & Astrophysics, University of Chicago, Chicago, IL 60637, USA

⁵ Department of Astronomy, Peking University, 100871, Beijing, China

⁶ Enrico Fermi Institute, The University of Chicago, Chicago, IL 60637, USA

* hliastro@umich.edu

tion and growing cluster particles over a few Myr. In contrast to all other cosmological simulations where stellar particles are formed instantaneously and only affect the formation of future particles, the formation of a stellar particle in our model is resolved in time and terminated by its own feedback. The final cluster masses are set self-consistently. Thus comparison of the model cluster mass function with observations allows us to constrain the star formation and feedback modeling.

In Section 2, we describe the simulation setup and detailed implementation of this sub-grid model. In Section 3, we examine the basic properties of the modeled clusters, e.g. CIMF and cluster formation efficiency, and compare these properties with recent observations of young massive star clusters in nearby galaxies. In Section 4, we discuss the origin of CIMF and the escape of ionizing radiation of young stars into the intergalactic medium. We summarize our conclusions in Section 5.

2. SIMULATION SETUP

The simulations were run with the Eulerian gasdynamics and N-body Adaptive Refinement Tree (ART) code (Kravtsov et al. 1997; Kravtsov 1999, 2003; Rudd et al. 2008). The latest version of ART includes several new physical ingredients that make it suitable for investigating the detailed star formation processes in a cosmological context. It includes an updated version of three-dimensional radiative transfer of ionizing and ultraviolet radiation using the Optically Thin Variable Eddington Tensor approximation (Gnedin & Abel 2001). Both the local ionizing radiation from star particles (Gnedin 2014) and the extra-galactic background (Haardt & Madau 2001) are considered as the ionization sources that feed into the radiative transfer solver. The ionization states of various species of hydrogen (HI, HII, H₂) and helium (HeI, HeII, HeIII), as well as the cooling and heating rates, are calculated based on the non-equilibrium chemical network. Finally, a phenomenological model of H₂ formation and self-shielding on dust grains (Gnedin & Kravtsov 2011) allows us perform a more realistic modeling of star formation based on local molecular component. ART has recently incorporated a subgrid-scale (SGS) model for the numerically unresolved turbulence. Turbulence, generated by gravitational accretion as well as kinetic feedback from stars and AGN, is an important ingredient for star formation (McKee & Ostriker 2007). This SGS model has been tested in isolated disk simulations (Semenov et al. 2015) and in this paper it is applied to cosmological simulations.

We run cosmological simulations in a periodic box of size $L_{\text{box}} = 4$ Mpc comoving. The initial condition is selected and tested by collisionless runs so that the central galaxy has total mass $M_{200} \approx 10^{12} M_{\odot}$ at $z = 0$. There are also a few satellite galaxies with total mass in the range $10^{10} - 10^{11} M_{\odot}$.

This initial condition has a non-zero ‘‘DC mode’’ that corrects the deviation of the cosmological evolution due to the difference between the average matter density in the box and the average matter density in the whole universe (Gnedin et al. 2011). A constant parameter Δ_{DC} , which represents the density fluctuation level of the current box, determines the relationship between the expansion rate of the box and the expansion rate of the universe:

$$a_{\text{box}} = \frac{a_{\text{uni}}}{[1 + \Delta_{\text{DC}} D_+(a_{\text{uni}})]^{1/3}}, \quad (1)$$

where a_{box} and a_{uni} are the scale factor of the simulation box and the global universe, respectively. $D_+(a)$ is the linear growth factor of density perturbation at scale factor a . Our

initial condition has $\Delta_{\text{DC}} = -1.02$, that is, a slightly underdense region.

The ART code uses adaptive mesh refinement, which increases spatial resolution in high density regions during simulation runtime. All of our simulations start with a 128^3 root grid, which gives the mass of dark matter particle $m_{\text{DM}} = 1.05 \times 10^6 M_{\odot}$ and size of the root cell 31.25 kpc comoving. We allow a maximum of ten additional refinement levels, which gives us spatial resolution of $L_{10} = 4 \times 10^6 / 128 / 2^{10} \approx 30$ pc comoving. At $z \sim 4$, the physical size of a level 10 cell is about 6 pc, smaller than a typical size of a giant molecular cloud. We employ a combination of the Lagrangian refinement criteria (both DM and gas mass) and the Jeans refinement criteria in the simulation. The cell will be refined if either criteria is fulfilled. For the Lagrangian refinement criteria, the cell will be refined if either the DM mass of the cell exceeds $3m_{\text{DM}}(\Omega_m/\Omega_{\text{DM}})f_{\text{tol}}$, or the gas mass exceeds $3m_{\text{DM}}(\Omega_b/\Omega_{\text{DM}})f_{\text{tol}}$, where the refinement split tolerance $f_{\text{tol}} = 0.6$. For the Jeans refinement criteria, cells larger than twice the local Jeans length λ_{Jeans} will be refined. The local Jeans length λ_{Jeans} is defined as

$$\lambda_{\text{Jeans}} = v_{\text{gas}} \tau_{\text{ff}} \approx \sqrt{\frac{\pi(c_s^2 + \sigma_v^2)}{G\rho_{\text{gas}}}}, \quad (2)$$

where c_s is the sound speed of the cell, and σ_v is the local gas velocity dispersion.

We adopt a Λ CDM cosmology with $\Omega_M = 0.304$, $\Omega_b = 0.048$, $h = 0.681$, and $\sigma_8 = 0.829$ that is consistent with the most recent *Planck* result (Planck Collaboration et al. 2015).

2.1. Continuous Cluster Formation

We introduce a new model for the formation of stellar particle in cosmological simulations: continuous cluster formation (CCF). In this prescription, cluster particles are formed within a spherical region of fixed physical size, $D_{\text{GMC}} \sim 10$ pc. This setup can avoid sudden changes of cell size by mesh refinement and gradual changes due to the expansion of the Universe.

Cluster particles are created only in cold ($T < T_{\text{crit}}$), dense ($\rho > \rho_{\text{crit}}$) cells with high molecular fraction ($f_{\text{H}_2} > f_{\text{H}_2, \text{crit}}$). New cluster particle can be created only in a cell that does not already contain another active particle. Otherwise we will grow the existing cluster instead of creating a new one. Also, we allow particle creation only when the spherical cluster formation region is located at the local density maximum by comparing the density of a given cell with its 6 immediate neighbors. Once created, active cluster particles will grow during the cluster formation timescale $\tau_{\text{max}} \sim 15$ Myr. Cluster particles with age older than τ_{max} will be labeled inactive and stop growing, because the observed age spread in young star clusters is typically below 10 Myr.

Since the resolution of the simulations can reach 30 comoving pc, a sphere of physical diameter 10 pc can be larger than a single cell at high red-shift. In this case, the neighbor cells that are covered by the sphere should also participate in cluster formation. We developed an algorithm that returns gas properties of central, as well as 26 neighboring cells, and calculates the total star formation rate (SFR) within the sphere. But the volume participating in cluster formation cannot be larger than the 27 cells.

The particle growth rate is calculated as follows. The SFR

Table 1
MODEL PARAMETERS

Models	SFE10 (fiducial)	SFE20	SFE100	LOWRHO	TURB50	TURBSF	TURBSF2
$\rho_{\text{crit}}(\text{cm}^{-3})$	1000	1000	1000	10	1000	-	-
$T_{\text{crit}}(\text{K})$	20000	20000	20000	20000	20000	-	-
$f_{\text{H}_2, \text{crit}}$	0.5	0.5	0.5	0.5	0.5	-	0.5
ϵ_{ff}	0.1	0.2	1.0	0.1	0.1	-	-
f_{turb}	0.1	0.1	0.1	0.1	0.5	0.5	0.5

Note. Other fixed parameters for all models: $\tau_{\text{max}} = 15$ Myr; $M_{\text{th}} = 10^3 M_{\odot}$; $D_{\text{GMC}} = 10$ pc; feedback speed ceiling $v_{\text{fb}}^{\text{ceiling}} = 5000$ km/s; feedback temperature ceiling $T_{\text{fb}}^{\text{ceiling}} = 10^8$ K.

density of the central cell is:

$$\dot{\rho}_* = \epsilon_{\text{ff}} \frac{f_{\text{H}_2} \rho}{\tau_{\text{ff}}}, \quad (3)$$

where $\tau_{\text{ff}} = \sqrt{3\pi/32G\rho_c}$ is the free-fall time of the central cell, and ϵ_{ff} is the star formation efficiency per free-fall time. The total mass accumulation rate within the sphere is the sum of the contribution from the central as well as 26 neighboring cells:

$$\dot{M} = \sum_i f_{\text{sp},i} V_i \dot{\rho}_{*,i} = \frac{\epsilon_{\text{ff}}}{\tau_{\text{ff}}} \sum_i f_{\text{sp},i} V_i f_{\text{H}_2,i} \rho_{\text{gas},i}, \quad (4)$$

where V_i is the volume of cell i , and $f_{\text{sp},i}$ is the fraction of V_i that is located within sphere. Here the SFR density of the neighboring cells is estimated by the free-fall time of the central cell, since the collapse of the whole spherical cluster formation region is dominated by the central cell. The mass increment during simulation timestep Δt is then $\Delta m = \dot{M} \Delta t$.

The star formation efficiency ϵ_{ff} in model SFE10 (fiducial) is set to be ten percent. Model SFE20 ($\epsilon_{\text{ff}} = 20\%$) and SFE100 ($\epsilon_{\text{ff}} = 100\%$) test the influence of the star formation efficiency on the global SFR as well as cluster particle properties. Recently, Padoan et al. (2012) found a relationship between ϵ_{ff} and the turbulent energy (e_{turb}) by analyzing MHD simulations of turbulent GMCs. Semenov et al. (2015) implemented a SGS turbulent model in the ART code by introducing additional terms into the momentum and energy equations to study the influence of turbulence on gas dynamics and explore the turbulence-dependent star formation efficiency in isolated disk simulations. In this paper, we setup a simulation TURBSF to test the SGS turbulent and the turbulence-dependent star formation efficiency model in cosmological runs. The SFR density is thus evaluated as $\dot{\rho}_* = \epsilon_{\text{ff}}(e_{\text{turb}})\rho/\tau_{\text{ff}}$. An artificial density threshold for star formation is not needed in this model, since it is implicitly included by the suppression of ϵ_{ff} in high temperature, strong turbulence medium. We also apply this turbulence-dependent star formation efficiency on molecular gas (TURBSF2) by adding the molecular fraction f_{H_2} in the above rate: $\dot{\rho}_* = \epsilon_{\text{ff}}(e_{\text{turb}})f_{\text{H}_2}\rho/\tau_{\text{ff}}$. The parameters of the runs are listed in Table 1.

For all simulations discussed in this paper, we take 10 pc, a typical size of dense clumps in GMCs, as the diameter of the cluster formation sphere, D_{GMC} . This value is consistent with the size of massive cluster-forming clouds that are observed in the recent sub-mm ATLASGAL survey (Urquhart et al. 2014). The range of the effective radius for massive proto-cluster candidates in that survey is about 5-10 pc. The value of D_{GMC} is tightly constrained. Any small sphere size would not contain enough material to form massive clusters,

while a significantly larger sphere size could include several regions that should be forming separate clusters.

If a cell is much smaller than the sphere, $L_{\text{cell}} < D_{\text{GMC}}/3$, the sphere will cover more than one layer of neighboring cells. Extracting gas properties of all cells within the sphere makes the book-keeping of the neighboring cells complicated and significantly reduces the computation efficiency. For that reason, we only allow cluster particles to grow their mass from the closest 27 cells. We performed a test run in which all 10 additional refinement levels are reached at high red-shift. At $z > 8$, the finest level has a cell size that is smaller than $D_{\text{GMC}}/3$. We find that the CIMF in this case does not exhibit a power-law shape any more and inconsistent with observations. This is possibly because that, when the sphere size is large enough to cover more than 27 cells, some fraction of the material within the sphere cannot participate cluster formation process in our algorithm. Therefore, we control the refinement criteria so that the smallest cell size is always larger than $D_{\text{GMC}}/3$. This suggests that gas cells are not allowed to reach the 10^{th} level of refinement until $z \lesssim 8$.

We also explored the possibility of varying sphere size based on the observed mass-size relation of local GMC (Larson 1981). However, it requires several iterations to obtain the appropriate cloud size and sometimes fails to converge. Another uncertainty comes from the normalization of the mass-size relation for GMCs in high- z environment. Therefore, we did not apply it in our current simulations.

As we mentioned above, if there exists an active cluster particle in a cell, the cluster mass will grow with the rate given by Eq. (4). The momentum and metallicity increment will also be added to the active particle accordingly. If there are more than one active cluster particles in a cell, we only grow the one with the smallest velocity relative to the host cell. This method prevents adding mass to unrelated cluster particles that occasionally fly through the cell. We also explored an alternative scenario of treating multiple active particles in a single cell by merging them into one active cluster. We found that the CIMF is no longer a power-law shape, but highly inclined toward high masses. This is possibly because that active clusters that fly from other cluster formation regions are absorbed by the main cluster, and clusters in different cluster formation clouds are merged.

Before creating a new cluster particle, we predict its mass during the formation timescale (τ_{max}) by assuming a constant SFR: $\dot{M}_{\text{est}} = \tau_{\text{max}} \dot{M}$. If this mass is smaller than a threshold mass M_{th} , the cluster particle will not be formed in order to avoid small-mass particles. After each global timestep, we delete all inactive cluster particles if their masses are smaller than M_{th} , and recycle their mass and momentum back to gas

cells. There are two reasons for this: to speed up the code and to avoid small-mass particles that would be artificially scattered by DM particles.

We would like to understand the accretion history of cluster particles. The typical timestep in our simulations is about 1000 years⁸. The active cluster formation period can be resolved by several thousand steps. Since it is not practical to store each local timestep, we record two integral timescales that characterize the mass accretion history. The first is the total duration of star-forming episode, $\tau_{\text{dur}} = t_{\text{end}} - t_{\text{creation}}$, where t_{creation} is the cosmic time of the creation of cluster particle and t_{end} is the last time before it becomes inactive. The second is the mass-weighted cluster formation timescale τ_{ave} :

$$\tau_{\text{ave}} = \frac{\int_{t_{\text{creation}}}^{t_{\text{end}}} (t' - t_{\text{creation}}) \dot{M}(t') dt'}{\int_{t_{\text{creation}}}^{t_{\text{end}}} \dot{M}(t') dt'}, \quad (5)$$

where $\dot{M}(t)$ is the mass accumulation rate of a given cluster particle at time t . By construction, the duration τ_{dur} cannot exceed the maximum formation time τ_{max} . For a constant \dot{M} , we expect $\tau_{\text{ave}} = \tau_{\text{dur}}/2$. If \dot{M} decreases over time, as a result of self-feedback of newly formed stars, we expect $\tau_{\text{ave}} < \tau_{\text{dur}}/2$. We discuss the accumulation history of star clusters in Section 3.5.

2.2. Dynamical disruption of star clusters

In the subsection above, we described the detailed implementation of the creation and growth of cluster particles. Another key ingredient, especially for the study of globular clusters, is their dynamical evolution. Star clusters suffer strong tidal destruction during the early stage when they are located within the gaseous disk, and experience internal evaporation after they escape to the galaxy halo. We create a new variable, the bound fraction f_{bound} , to represent the fraction of mass that is still bound to the cluster particle, and update f_{bound} based on the local tidal field as well as the internal evaporation. We use Eq. (3) of Gnedin et al. (2014) to estimate the mass loss rate of star clusters (dM/dt). Since this paper mainly focuses on the formation processes of young star clusters, we will not discuss the details of the method of calculating cluster bound fraction, and leave this topic to a follow-up paper.

2.3. Stellar Feedback

The creation of cluster particles is followed by stellar feedback that returns mass, momentum, and energy into the surrounding medium. The feedback process has been demonstrated to be crucial in maintaining steady star formation activity.

The sub-grid stellar feedback model used in our simulations is similar to that described in Agertz et al. (2013). It includes the injection of thermal energy, momentum, metals, and ionization radiation from supernova (SN) explosion, stellar winds, stellar luminosity, and radiative pressure onto surrounding gas and dust. The SN rate of a given cluster particle is calculated by assuming the Kroupa initial mass function (Kroupa 2001), and the injected energy and momentum are

⁸ For a gas cell with size $L_{\text{cell}} = 10$ pc, Courant-Friedrichs-Lewy condition requires a timestep smaller than $\Delta t < L_{\text{cell}}/v_{\text{gas}} = 10^4 \text{ yr } (L_{\text{cell}}/10 \text{ pc}) (v_{\text{gas}}/1000 \text{ km/s})^{-1}$. Due to the discreteness of the timestep refinement among various levels, the timestep at the highest level is even shorter if it is passed from lower level cells with high velocity and high temperature. We find that the typical timestep for our fiducial run is about 1000 yr.

calibrated by Padova stellar evolution models (see details in Agertz et al. 2013). An analytical fit by Gnedin (2014) is used to account for the time evolution of the ionization radiation from young stars. During the growth of active cluster particles, we use the mass-weighted age as the age of the stellar population, which determines the amount of feedback. We also include the SGS turbulence model that treats the unresolved turbulent energy as a separate hydrodynamic variable. This is similar to the “feedback energy variable” in Agertz et al. (2013), but here the turbulent energy is solved by the hydro solver with sophisticated treatment on the processes such as turbulent pressure, viscosity, and diffusion (see details in Semenov et al. 2015).

The momentum exerted from stellar particles is distributed evenly to 26 nearest neighbors surrounding the parent cell of the stellar particles. The feedback momentum is added directly into the cell if it has the same direction with the momentum of that cell. Otherwise, the feedback momentum is subtracted from the cell momentum and the kinetic energy associated with the canceled momentum is converted to thermal energy and added to the cell internal energy. When adding feedback energy or momentum onto a given cell, we also check whether the temperature (or velocity) of the cell is larger than $T_{\text{fb}}^{\text{ceiling}} = 10^8$ K (or $v_{\text{fb}}^{\text{ceiling}} = 5000 \text{ km/s}$). To avoid creating unrealistic hot and fast flow, feedback does not add to cells whose temperature or velocity has already reached the ceiling value.

Although the feedback model contains many physical ingredients from various sources, it should be noted that the only adjustable parameter is the fraction of SN energy that is converted into turbulent energy, f_{turb} . In the fiducial run, we set $f_{\text{turb}} = 10\%$ and we vary this factor to 50% in TURB50 model to test the effect of turbulence on our results.

3. RESULTS

The simulations stall at low red-shift because of the very short timestep. Our fiducial run has reached $z=3.3$ and most of the results about it are from this snapshot. We use the ROCK-STAR halo finder (Behroozi et al. 2013b) to identify halos and substructures in the whole simulation box, and construct halo merger trees by the consistent-tree algorithm (Behroozi et al. 2013c).

Figure 1 shows the gas density projection plots of the main galaxy for the fiducial run at $z \sim 3.3$ in three different scales from 400 kpc to 4 kpc. The filamentary structure that connects galaxies is clearly seen in the left panel. In the central panel, the gaseous disk of the main galaxy is shown in a face-on view, with obvious spiral patterns. There are also substructures orbiting the main galaxy, including significant tidal streams. In the right panel, the simulation is zoomed in to 4 kpc, and the discreteness of outer gas cells becomes visible. In the outer edge of the galaxy, the density is low and the mesh is coarse, while at the center, the highest refinement level is reached due to the high density.

3.1. Star formation histories

Figure 2 shows the star formation history (SFH) of the main galaxy for different models, compared to the SFH of $M_{\text{vir}}(z=0) = 10^{12} M_{\odot}$ halo derived from the abundance matching technique (Behroozi et al. 2013a). The star formation history is calculated from all cluster particles in the main galaxy at the last snapshot smoothed over 100 Myr.

All models show similar SFH that rises towards lower red-shift with periodic bursts of star formation. The overall rate of

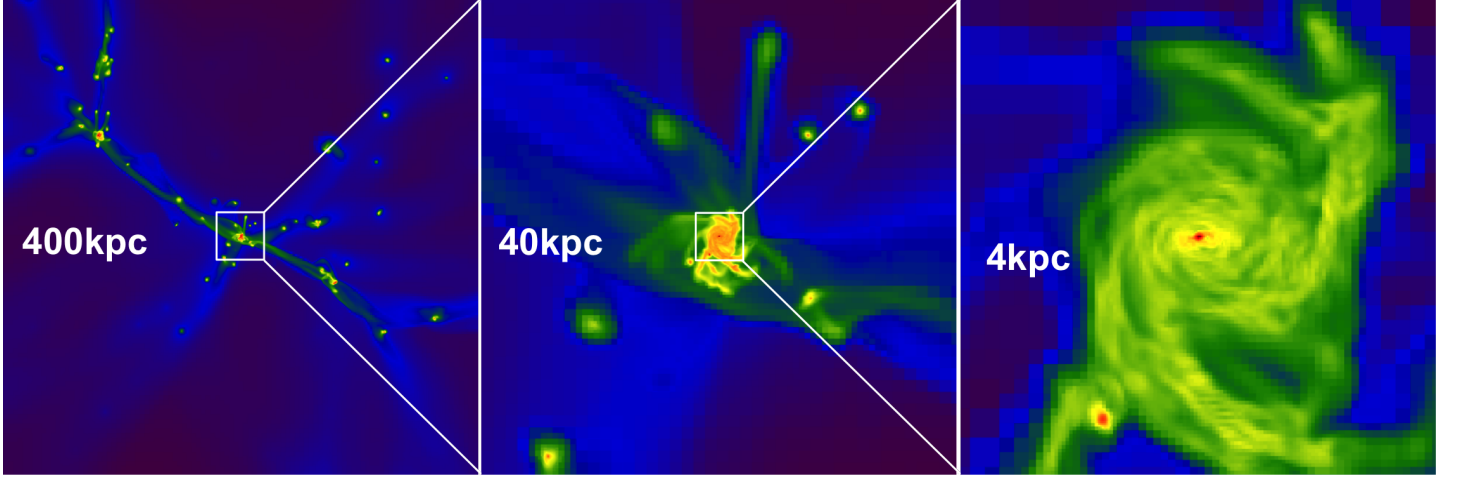


Figure 1. Gas density projection plots of the fiducial run centered on the main galaxy at $z \sim 3.3$. The physical sizes of box for the three panels, from left to right, are 400 kpc, 40 kpc, and 4 kpc, respectively.

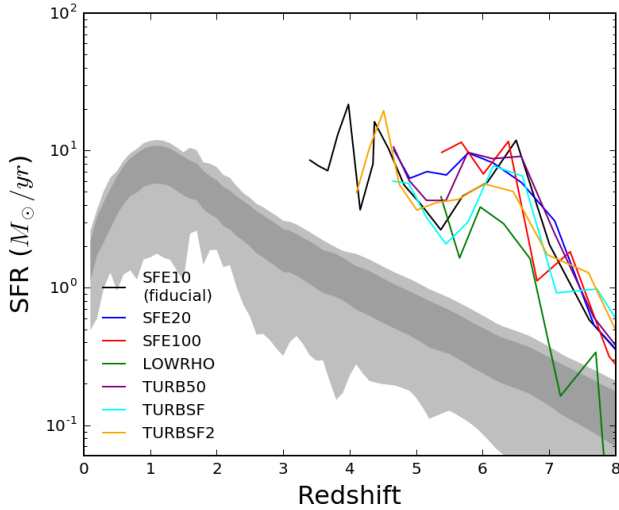


Figure 2. Simulated star formation history of the main galaxy, smoothed over 100 Myr bins, for different models (see legend). The star formation history for a $M_{\text{vir}}(z=0) = 10^{12} M_{\odot}$ halo from the abundance matching technique (Behroozi et al. 2013a) is overplotted by shaded regions. The dark and light regions show the one- and two-sigma confidence intervals, respectively.

star formation in our simulations is not sensitive to the model parameters such as ϵ_{ff} and f_{turb} . This is possibly because feedback regulates star formation activity. However, it seems that the feedback in our simulations is not strong enough to match the average SFR predicted by Behroozi et al. (2013a). We still need to investigate whether this high SFR is due to the implementation of feedback processes, or the specific initial condition we chose for these runs. Recent FIRE simulations show that SFH depends not only on feedback scheme but also on the initial condition (Hopkins et al. 2014). For example, their run m12q shows higher SFR at high redshift due to the “quiescent” nature of the initial condition.

Another important global property of galaxies that links star formation and molecular gas is the gas depletion timescale. It is defined as the timescale to consume all molecular gas with current SFR: $\tau_{\text{dep}} = M_{\text{mol}}/\text{SFR}$. The typical value of τ_{dep}

in nearby disk galaxies is found to be 2.35 Gyrs (e.g. Bigiel et al. 2008). Recent surveys on the active star-forming galaxies out to $z = 3$ suggest a decreasing gas depletion timescale toward higher redshift (Tacconi et al. 2013; Saintonge et al. 2013; Genzel et al. 2015). Estimating the SFR and molecular gas surface density for high redshift galaxies is still challenging. Aravena et al. (2016) use ATCA and ALMA measurements to estimate τ_{dep} for dusty lensed galaxies at $z = 4-6$, and find the range of 10-100 Myr, much smaller than that in low redshift galaxies.

We calculate the total molecular gas mass and the SFR for the main and satellite galaxies in our fiducial run, and estimate τ_{dep} at various epochs from $z \sim 3.3-6.7$. The derived τ_{dep} is in the range of 20-600 Myr, with a mean value ~ 160 Myr, consistent with the observed high redshift samples.

3.2. Cluster initial mass function

One of the most fundamental properties of young star clusters is the CIMF. Observations of nearby galaxies have found that CIMF follows a Schechter form: a power-law distribution with an exponential cutoff at M_{cut} (see Portegies Zwart et al. 2010, and references therein):

$$\frac{dN}{dM} \propto M^{-\alpha} \exp(-M/M_{\text{cut}}), \quad (6)$$

where the power-law index $\alpha \approx 2$. The typical value of M_{cut} for Milky Way-sized spiral galaxies is about $2 \times 10^5 M_{\odot}$ (e.g. Gieles et al. 2006), and $M_{\text{cut}} > 10^6 M_{\odot}$ for luminous interacting galaxies (Bastian 2008). Figure 3 shows the model CIMF in main galaxy for the fiducial run. The CIMF exhibits a Schechter-like shape with power-law slope similar to the observed. However, CIMF at different epochs shows different normalization and cutoff mass, which are both correlated with SFR.

To investigate the relationship between SFR and the high mass end of the CIMF, we split the whole cluster sample into several bins based on cluster ages. We take bins of 50 Myr, and, for each bin, we estimate the average SFR, maximum cluster mass (M_{max}), and the best-fit power-law slope and M_{cut} . The average value of the best-fit slope for all bins is $\alpha \approx 1.8$, similar to the observed. In Figure 4, we find a strong correlation between the SFR and M_{max} , as well as M_{cut} , for bins with $\text{SFR} > 1 M_{\odot}/\text{yr}$. The best-fit relationship between

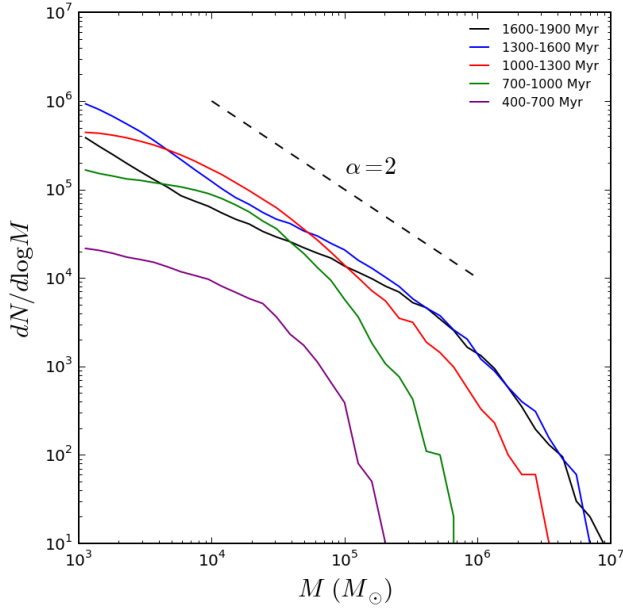


Figure 3. Cluster initial mass function for different cluster age bins in the main galaxy for the fiducial run. A power-law distribution with slope of 2 is plotted by a dashed line. The mass functions exhibit a stable shape across a large range of cosmic time, and both the power-law slope and the high mass cutoff are consistent with observed cluster samples in nearby galaxies.

SFR and M_{cut} is:

$$M_{\text{cut}} \approx 1.4 \times 10^4 M_{\odot} \left(\frac{\text{SFR}}{1 M_{\odot}/\text{yr}} \right)^{1.6}, \quad (7)$$

and the relationship between SFR and M_{max} is:

$$M_{\text{max}} \approx 8.8 \times 10^4 M_{\odot} \left(\frac{\text{SFR}}{1 M_{\odot}/\text{yr}} \right)^{1.4}. \quad (8)$$

Theoretically, for samples drawn from any given mass function dN/dM , M_{max} can be calculated by the integral equation:

$$1 = \int_{M_{\text{max}}}^{\infty} \frac{dN}{dM} dM. \quad (9)$$

Comparing the estimated M_{max} with the actual value can help us determine the shape of CIMF.

For the case of pure power-law CIMF without intrinsic exponential cutoff, $dN/dM = M_0 M^{-\alpha}$, M_{max} can be estimated by:

$$1 = \int_{M_{\text{max}}}^{\infty} \frac{dN}{dM} dM = \int_{M_{\text{max}}}^{\infty} M_0 M^{-\alpha} dM, \quad (10)$$

which gives $M_0 = (\alpha - 1) M_{\text{max}}^{\alpha-1}$. The total mass of star clusters is thus evaluated as:

$$M_{\text{tot}} = \int_{M_{\text{min}}}^{M_{\text{max}}} M \frac{dN}{dM} dM = \begin{cases} M_{\text{max}} \ln \frac{M_{\text{max}}}{M_{\text{min}}} & \text{if } \alpha = 2 \\ \frac{(\alpha - 1)(M_{\text{min}}^{2-\alpha} - M_{\text{max}}^{2-\alpha})}{(\alpha - 2)M_{\text{max}}^{1-\alpha}} & \text{otherwise} \end{cases} \quad (11)$$

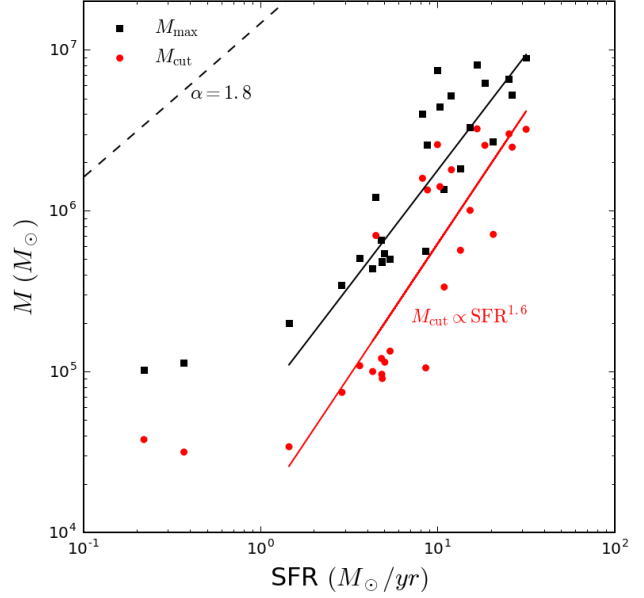


Figure 4. SFR vs. maximum cluster mass (M_{max}) and cutoff mass (M_{cut}) for the fiducial run. The SFR is averaged over 50 Myr and M_{max} is chosen from the clusters found in the same time interval. The initial mass function of clusters in each interval is fitted by Eq. (6), and both the power-law slope and cutoff mass are obtained. The red solid line shows the best-fit relation between M_{cut} and SFR for samples with $\text{SFR} > 1 M_{\odot}/\text{yr}$. The theoretical maximum masses for given SFRs for both the pure power-law and Schechter shape mass function are shown by dashed and solid black lines, respectively (See Section 3.2 for detail calculations). Note that the black solid line is not the best-fit between SFR and M_{max} , but the expected M_{max} by assuming a Schechter CIMF with $\alpha = 1.8$ and M_{cut} that is estimated by the empirical M_{cut} -SFR relation (red line).

For a given SFR, M_{tot} is simply the SFR times the bin size 50 Myr, and M_{max} can be obtained by solving Eq. (11) with $\alpha = 1.8$ and $M_{\text{min}} = 10^3 M_{\odot}$. From Figure 4, we can see that the theoretical M_{max} overestimates the actual maximum cluster mass by more than one order of magnitude.

Alternatively, for the case of Schechter-like CIMF as described by Eq. (6), the relationship between M_{tot} and M_{max} is:

$$M_{\text{tot}} = \frac{\Gamma(2 - \alpha, M_{\text{min}}/M_{\text{cut}}) - \Gamma(2 - \alpha, M_{\text{max}}/M_{\text{cut}})}{\Gamma(1 - \alpha, M_{\text{max}}/M_{\text{cut}})} M_{\text{cut}}, \quad (12)$$

where $\Gamma(s, x)$ is the upper incomplete Gamma function. With $\alpha = 1.8$ and the relationship between SFR and M_{cut} in Eq. (7), the expected M_{max} can be obtained by solving Eq. (12) numerically. It should be emphasized that the black solid line in Figure 4 is not the best-fit relation between SFR and M_{max} , but the expected M_{max} calculated from the above procedure. The similarity between this expected M_{max} and the one obtained from the simulations suggests that the Schechter function is an excellent representation of the CIMF in our simulation, and pure power-law distribution is ruled out.

Another interesting aspect of about CIMF is its spatial variation. Recently, Adamo et al. (2015) examined the mass function of young star clusters in M83 using multiband *Hubble Space Telescope* imaging data. They split the whole M83

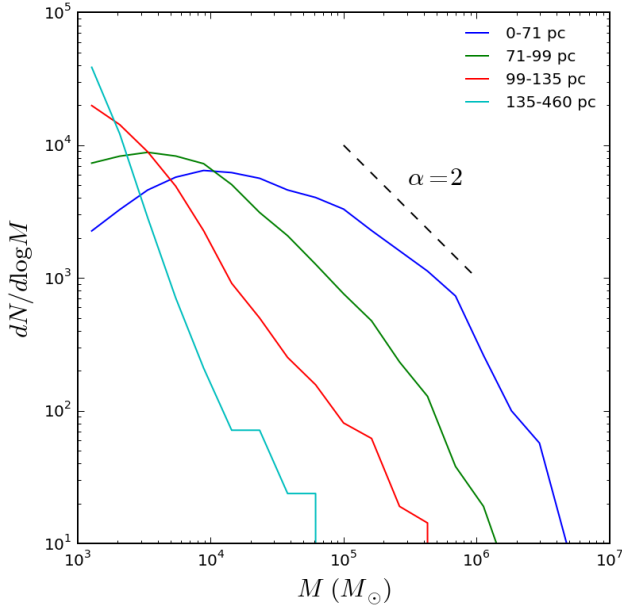


Figure 5. Initial mass function of young clusters (<100 Myr) in four radial bins of equal cluster number for the main galaxy in the fiducial run. The mass functions shows a clear steepening from the inner annulus (bin1, blue line) to the outer ones (bins 2, 3 and 4 as the radius of the annulus become larger). The corresponding radius ranges in physical unit for the four bins are listed in the legend.

cluster sample into four radial bins and found a significant steepening of the CIMF in the outer bins. Following a similar procedure, we divide our main galaxy at $z \approx 3.3$ by four concentric circles so that each annulus contains the same number of star clusters with age younger than 100 Myr. The CIMF of each bin is shown in Figure 5. The mass function no longer has a universal shape, but presents a spectrum of power-laws with various slope: the inner bins ($R < 100$ pc) have CIMF that has slopes smaller than -2 , and the outer bins ($R > 100$ pc) larger than -2 in the mass range of $10^3 - 10^5 M_\odot$. The trend of the CIMF steepening as a function of galactocentric distance is consistent with the spatial variation of CIMF in M83. Moreover, the maximum mass of clusters in the inner bins is much higher than that in the outer ones. The SFR density for the four bins from inner to outer ones is 460, 14, 0.06, and $0.02 M_\odot/\text{yr}/\text{kpc}^2$. It is clear that the gradient of CIMF correlates with the local SFR density. It is a local manifestation of the global trend shown in Figure 4.

Finally, we explore the variation of CIMF under different model parameters. In Figure 6, we show the CIMF of all models in the main galaxy at the same epoch ($z \approx 5.3$). Models TURB50 and SFE20 present similar CIMF to the fiducial run, indicating that our CCF prescription is not sensitive to model parameters when they are in a reasonable range. Model SFE100, with one hundred percent star formation efficiency per free-fall time, on the other hand, has a CIMF that is dramatically different. Its CIMF deviates from a power-law distribution, and has a truncation mass that is much lower than the other runs. Although the inability to create massive clusters with a very high star formation efficiency seems counter-intuitive, it reflects the complex nature of the interplay between star formation and feedback: very high star formation

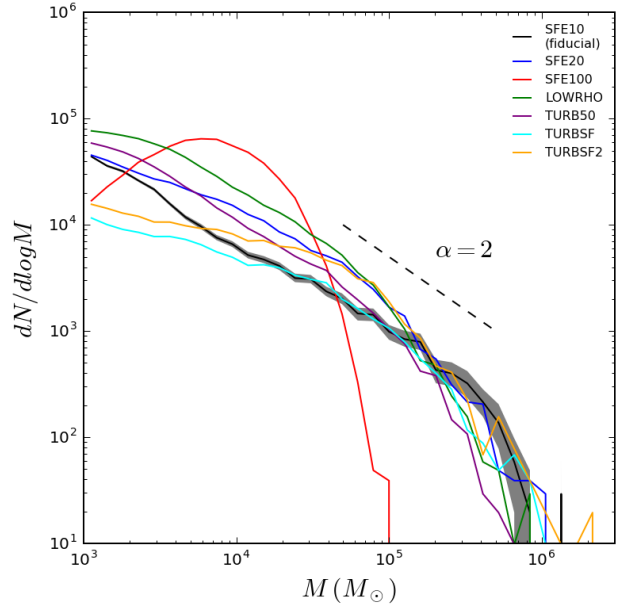


Figure 6. Cluster initial mass function of all seven models (see legend for color codes) in the main galaxy at the same epoch ($z \sim 5.3$). The grey shaded region around the black line is the 95% confidence interval of the CIMF constructed by bootstrap resampling for the SFE10 model (fiducial).

efficiency leads to an early starburst; subsequent stellar feedback from this initial burst is strong enough to destroy molecular gas and expels material from the star-forming region; in a short time, the cluster growth is terminated and the final cluster mass is determined only by the first episode of starburst. This scenario is confirmed by analyzing the cluster formation timescales in Section 3.5.

3.3. Major merger and massive cluster formation

To investigate the environmental dependence on the CIMF, we plot in Figure 7 the relationship between the star formation history of the main galaxy and the major merger events of the host halo. The SFR is split in two parts contributed by low-mass and high-mass clusters. The merger ratio is defined as the differential increase of the main halo mass between adjacent snapshots: $R_m = (M_{h,i} - M_{h,i-1})/M_{h,i}$, where $M_{h,i}$ is the halo mass of the main halo in the i^{th} snapshot. The progenitor and descendant information of the main halo is extracted from the merger tree calculated by ROCKSTAR. Only mergers with $R_m > 0.3$ are present in the figure, and the duration of the two major merger events is determined by visual check of the DM density distribution across several snapshots. Quantitatively, we set the starting point of a major merger by the time when the host-satellite separation becomes less than ~ 30 kpc, following Scudder et al. (2012) who found a systematic enhancement of SFR for galaxy pairs with projected separation smaller than 30 kpc. We can see that the last major merger with merger ratio $R_m \sim 0.6$ at $z \sim 4-5$ triggers starbursts with SFR peaks around $50 M_\odot/\text{yr}$, and creates a large fraction of clusters more massive than $5 \times 10^4 M_\odot$.

To investigate possible differences in the shape of CIMF during major mergers and during quiescent periods, we split the model clusters into major-merger-generated ($t_{\text{creation}} =$

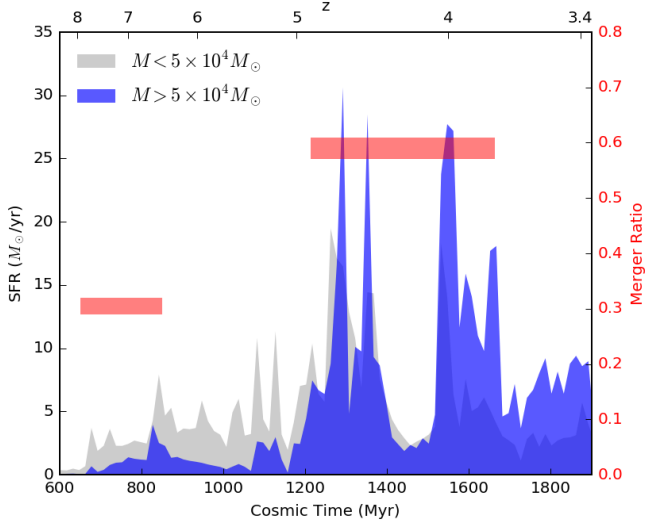


Figure 7. Star formation history of the main galaxy split into massive (blue shaded; $M > 4 \times 10^4 M_\odot$) and less massive components (gray shaded; $M < 4 \times 10^4 M_\odot$) for the fiducial run. Two major merger events with merger ratio larger than 0.3 are labeled by red bars. The duration of each major merger events is represented by the length of the bar, while the merger ratio that is derived from the merger tree information is indicated by the height of the bar with scale that is shown in the right y-axis label.

1250–1400 Myr) and non-major-merger-generated ($t_{\text{creation}} = 900 - 1200$ Myr) groups. From Figure 8, we find that the cluster mass distribution has higher cutoff mass during major merger event so that the maximum mass extends to higher value. This can be understood by the empirical $\text{SFR} - M_{\text{cut}}$ relation described by Eq. (7). In non-major merger case, the typical SFR is about $5 M_\odot/\text{yr}$ and the corresponding cut-off mass is $1.8 \times 10^5 M_\odot$, while in major merger case, $M_{\text{cut}} = 1.7 \times 10^6 M_\odot$ for $\text{SFR} = 20 M_\odot/\text{yr}$. Physically, this is consistent with the picture of the formation of massive star clusters in high-pressure environment that is produced by major mergers (Kruijssen 2014; Renaud et al. 2015).

3.4. Fraction of clustered star formation

We investigate the relationship between SFR surface density and the fraction of clustered star formation. It is defined as the fraction of all star formation contained in clusters more massive than a chosen minimum mass M_{cl} :

$$\Gamma = \frac{\text{SFR}(M > M_{\text{cl}})}{\text{SFR}}. \quad (13)$$

We split the main and satellite galaxies into various concentric circular bins, as we did to study the spatial variation of CIMF in Section 3.2. We calculate the SFR surface density by dividing the SFR by the area of the annulus. We calculate the SFR by counting all cluster particles in a given annulus with ages between 15 to 50 Myr and use $M_{\text{cl}} = 10^4 M_\odot$ to calculate Γ , similar to the choice that is used in the study of star clusters in M83 (Adamo et al. 2015).

Figure 9 shows the relationship between the SFR surface density and Γ from the fiducial run at $z \approx 3.3$. The trend that higher Σ_{SFR} leads to higher Γ is reproduced in our model over a large range of Σ_{SFR} from 10^{-4} to $10^3 M_\odot/\text{yr}/\text{kpc}^2$. To test the robustness of this result, we vary M_{cl} from $5 \times 10^3 M_\odot$ to

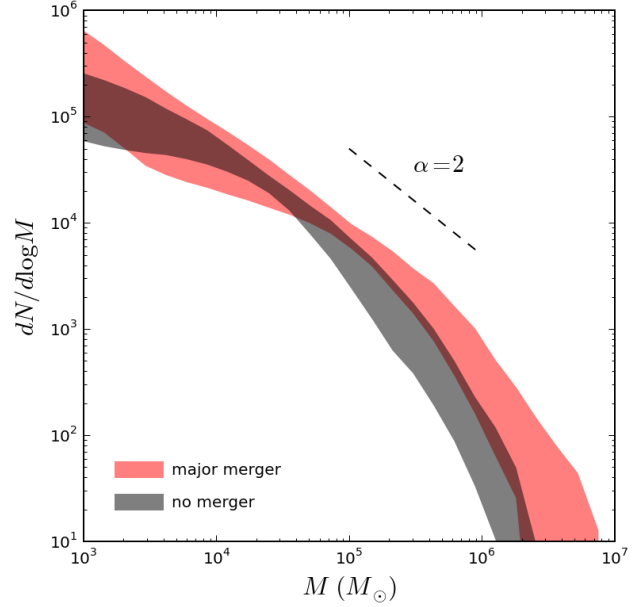


Figure 8. Cluster initial mass function split by merger activities: the mass function during major merger $t_{\text{creation}} = 1250 - 1400$ Myr (black) and between mergers $t_{\text{creation}} = 900 - 1200$ Myr (red). Each band shows the standard deviation of the mass functions around the mean value of models SFE10 SFE20, TURB50, TURBSF, and TURBSF2.

$10^5 M_\odot$ and find that, although the absolute value of Γ changes with M_{cl} , the positive correlation remains. We also find that, for the same galaxy, both Σ_{SFR} and Γ are higher for inner annuli than outer ones. This can be understood by the spatial variation of the CIMF as we discussed in Section 3.2. The shallower slope, as well as the higher cutoff mass, of the CIMF in the inner annuli naturally leads to a higher Γ than the outer ones.

3.5. Cluster formation timescale

Recent observations of nearby massive star-forming regions suggest that cluster formation process is quick (Lada & Lada 2003). Hartmann et al. (2012) compile age information of young stars in Orion Nebula Cluster and find the age spread as short as only a few Myr. We investigate the formation timescale and mass accretion history of the model clusters by analyzing the distribution of two characteristic timescales, τ_{dur} and τ_{ave} , defined in Section 3.5. In Figure 10, we plot the cumulative probability distribution of τ_{dur} and τ_{ave} of all cluster particles in the main galaxy for all models at $z \approx 5.3$. As can be seen from the left panel, most cluster particles stop accretion completely within 10 Myr for models SFE10, SFE20, SFE100, and TURB50. For model SFE100, majority of the cluster particles become inactive within only 4 Myr. This is because feedback from active cluster particles heat up and blows out the gas from their natal GMCs and change the cell properties so that one or more star formation criteria are violated. For two turbulence-dependent star formation efficiency models, TURBSF and TURBSF2, star clusters are not able to completely shut down accretion until very long time because there is no artificial density threshold that is assigned to turn off star formation. So, even if the feedback from cluster particle has already blown out majority of the nearby molecular

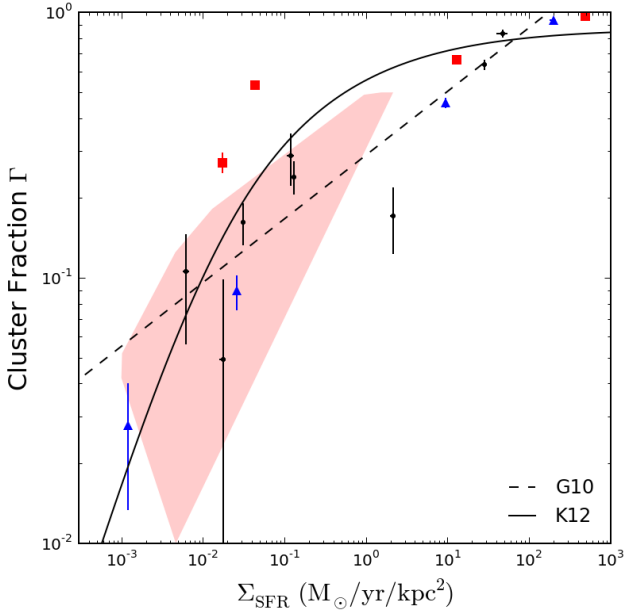


Figure 9. SFR density vs. fraction of clustered star formation in both the main and satellite galaxies for the fiducial run at $z \approx 3.3$. Using the same method when investigating the spatial variation of the mass function in Section 3.2, the simulated galaxies are cut into various radial bins. The SFR density of each bin is estimated by dividing SFR by the area of the bin and the cluster fraction is defined as the mass fraction of cluster particles with masses larger than $10^4 M_\odot$. Only young clusters with age between 15 to 50 Myr are selected. The red and blue points represent the clusters in the main and the second largest galaxies, respectively. Dashed line shows the empirical relation from observed star cluster populations in 7 nearby galaxies by Goddard et al. (2010), while the red shaded region shows an envelop that covers the data points that are compiled in Adamo et al. (2015). The theoretical predicted $\Sigma_{\text{SFR}}-\Gamma$ relation from (Kruijssen 2012) is also overplotted here by solid line.

gas, there is still a trickle of mass that can be added to the cluster particle.

A more physical estimate of the cluster formation timescale is the mass-weighted value, τ_{ave} , which contains the information of the mass accretion history of individual cluster, see Eq. (5). On the right panel, the timescales of TURBSF and TURBSF2 models are much shorter and more than 50% of the cluster particles assemble their masses within 5 Myr. For the fiducial run, most of the cluster particles have τ_{ave} smaller than 4 Myr, consistent with observations.

Another feature of the plot is the dependency of the cluster formation timescale on the star formation efficiency. It is clear in both panels that, the higher the star formation efficiency ϵ_{ff} , the faster the cluster are formed. In the case of SFE100, more than 50% of the cluster particles are formed within only 1 Myr.

Although it is impractical to store mass increases of all cluster particles at each local timestep, we randomly select several active clusters with mass larger than $10^5 M_\odot$ and write out the mass growth history during their active periods. The goal is to check whether the conclusions drawn from τ_{dur} and τ_{ave} are consistent with this detailed output. We normalize the mass evolution of each cluster by its final mass M_{final} , split the τ_{max} into 100 intervals of equal size, and calculate the mean and

variance of $M(t)/M_{\text{final}}$ at each interval. The average cluster formation history, together with the amount of variation, is shown in Figure 11. The mean cluster accretion history is well described by a decreasing accretion rate, $\dot{M} \propto t^{-1/2}$, and deviates from both constant and linearly increasing accretion rates. In fact, this decreasing trend has already been reflected from the very short τ_{ave} found in Figure 10.

From the large scatter shown in Figure 11, we conclude that different clusters have dramatically different growth history during their active period. This reveals intricate physical conditions of the star-forming regions in different places of the galaxy and the complex interplay between gas accretion and stellar feedback from the host as well as nearby clusters.

We also performed a test run with all the feedback sources turned off. The average mass accretion history in the non-feedback case is closer to the constant accretion rate line and shows less variation than that in the feedback case.

3.6. Escape of ionizing radiation

Young stars in massive star clusters produce copious amount of ionizing radiation that travels through the interstellar medium and may potentially leave the host galaxy. The escaped radiation would contribute to the extragalactic UV flux that reionized the universe by red-shift ~ 6 (e.g. Gnedin 2016). Before this radiation escapes the galaxy, a significant portion will be absorbed by neutral hydrogen located close to the stellar sources. Since stellar radii cannot be resolved in a cosmological simulation, calculation of the escape fraction depends on the numerical resolution. Our simulations reach smaller cell size than most current galactic simulations, and therefore, can provide a useful estimate of the escape fraction in the inner few hundred parsecs. We calculate the absorption by neutral hydrogen using the absorption cross-section integrated over the radiation spectrum, separately for atomic hydrogen and molecular hydrogen. These cross-sections are about 3 times lower than the monochromatic cross-sections at the ionization edge:

$$\sigma_{\text{HI,int}} = \int \sigma_{\text{HI}}(\nu) f_\nu d\nu \bigg/ \int f_\nu d\nu = 0.34 \times \sigma_{\text{HI}}(13.6\text{eV}) \quad (14)$$

$$\sigma_{\text{H}_2,\text{int}} = 0.36 \times \sigma_{\text{H}_2}(15.4\text{eV}) \quad (15)$$

We take $\sigma_{\text{HI}}(13.6\text{eV}) = 6.3 \times 10^{-18} \text{cm}^2$, and $\sigma_{\text{H}_2}(15.4\text{eV}) = 10^{-17} \text{cm}^2$. The total optical depth for absorption is $\sigma_{\text{HI,int}} N_{\text{HI}} + \sigma_{\text{H}_2,\text{int}} N_{\text{H}_2}$. The total escape fractions at the virial radius are very small, $f_{\text{esc}} \sim 10^{-6} - 10^{-4}$, independent of galaxy mass. The escape fraction correlates with the star formation rate, $f_{\text{esc}} \sim 10^{-6}$ for $\text{SFR} < 1 M_\odot/\text{yr}$, and $f_{\text{esc}} \sim 10^{-4}$ for $\text{SFR} > 2 M_\odot/\text{yr}$, at $z = 6$. Our simulations include the extragalactic background contribution to the UV flux (Haardt & Madau 2001) which dominates the internal flux outside 2 kpc from the galaxy center. Therefore, the simulations are better suited to calculate the escape fraction in the inner parts of the host galaxies. For example, the CROC simulations (Gnedin 2014) compute the escape of ionizing radiation from the inner cell size of 875 comoving pc. Our highest-resolution cell is 15 times smaller. To estimate the internal absorption within one CROC cell, we calculated the escape fractions from the sources to a distance of 875 pc, azimuthally averaged. They range from 10^{-8} to 10^{-2} . They never exceed 1% in our simulations, which indicates that the absorption in the immediate environment of stellar sources is very strong.

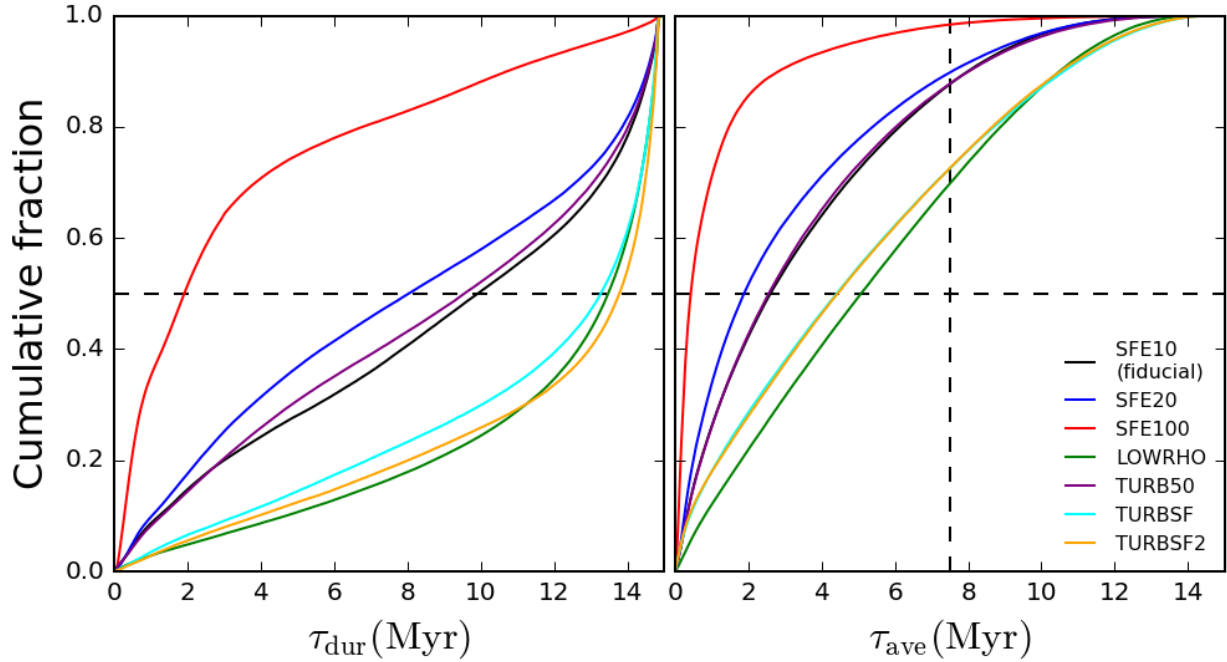


Figure 10. Cumulative distribution function of the cluster formation duration τ_{dur} (left panel) and the mass-averaged cluster formation timescale τ_{ave} (right panel). Difference colors show the distribution for different models, see legend for details. The cluster samples are selected within the main galaxy at $z \approx 5.3$ for all models.

4. DISCUSSION

4.1. Comparison with other star formation implementations

Most cosmological simulations use the star formation implementation that is similar to Katz (1992): a fraction of cold and dense gas is converted to star particles with a constant star formation efficiency. Some simulations use a fixed star particle mass and create particles with a Poisson random process at each timestep, others use a relatively long star formation sampling timescale (typically several Myrs) and create star particles with varying masses. In contrast, Cen & Ostriker (1992) create and evolve star particles following a given analytical mass accretion history out to the local dynamical time. However, as we can see in Section 3.5, the mass accretion history of individual cluster particles in our simulations varies dramatically and a simple analytical expression is insufficient. Moreover, in all above methods, star particles are created instantaneously and the particle masses are determined before their feedback processes start to influence the ambient environment. In our model, however, cluster particles grow their mass continuously at each local timestep until their own feedback terminates the mass growth. The mass accumulation history is resolved by a large number of timesteps, and the final cluster mass is obtained self-consistently so that it can be considered as a good proxy of the mass of cluster formed from a given star formation region.

Another branch of star formation modeling is the sink particle approach, which is widely used in the star and planet formation community for both SPH (e.g. Bate et al. 1995) and mesh-based (Krumholz et al. 2004; Federrath et al. 2010) codes. In this approach, a sink particle is created if the gas condition matches several criteria. A spherical accretion region around the sink particle is introduced right after the particle creation, similar to our cluster-forming sphere. But they

grow a sink particle from all the gas above the threshold density, whereas we use all gas mass (only as long as it is above the threshold) within the sphere to estimate SFR. Particles in our model grow slower, over a period of time specified by the parametrized physics of star formation based on observations of individual GMCs that is compatible to our spatial resolution (Krumholz et al. 2012). On the other hand, the sink particle approach usually requires a much higher spatial resolution so that the star formation region can be resolved by many gas cells in order to determine various accretion properties, such as the flow convergence and mass increment at each timestep. In cosmological simulation, however, spatially resolving cluster-forming regions requires a sub-pc spatial resolution, which is still computationally challenging.

4.2. On the shape of CIMF

In Section 3.2, we examined our model CIMF in different galaxies at various epochs and found that it can be well described by a Schechter function. The power-law index is also consistent with observations. It is interesting to investigate the physical origin of the shape of the CIMF and the connection between the cluster mass and the physical properties of the interstellar medium.

In Figure 12, we plot the mass function of various quantities related to cluster particles. Since cluster particles in our model is formed within cluster-forming spheres, we estimate a rescaled total (molecular) cell mass by multiplying the total (molecular) density of gas cells by the volume of the cluster-forming sphere. The distribution of this rescaled total (molecular) cell mass exhibits a very steep slope at lower masses and deviates from the CIMF dramatically. We also calculate the exact molecular gas mass within cluster-forming spheres by summing over contributions from the central cell as well as 26 neighbors: $M_{\text{sp}} = \sum f_{\text{sp},i} V_i f_{\text{H}_2,i} \rho_{\text{gas},i}$. The mass function of

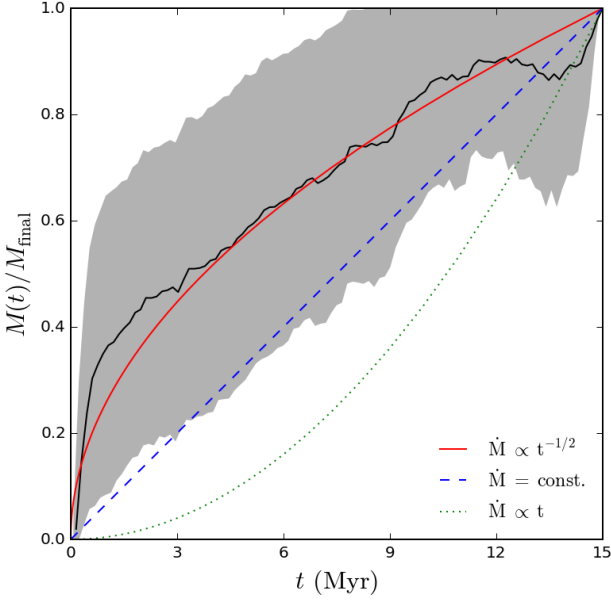


Figure 11. Average cluster accretion history for randomly selected active clusters for the fiducial run. Mass growth of a given cluster at each local timestep is normalized by its final mass, the average cluster accretion history (black solid line) is estimated by the averaged normalized mass within each time interval. The large variation of the mass growth history is presented by the grey region. Three analytical accretion histories with decrease, constant, and increase accretion rate are overplotted with red solid, blue dashed, and green dotted lines, respectively. The average cluster accretion history is well described by a decreasing accretion evolution, $\dot{M} \propto t^{-1/2}$.

M_{sp} shows a slope that is closer to the slope of the CIMF. This implies that our method in which the sphere encloses gas cells with various density is a better way of simulating star cluster formation. However, the power-law slope of the sphere mass function is still steeper than the slope of the CIMF, and the maximum mass is $\sim 2 \times 10^6 M_{\odot}$, several times smaller than the maximum mass of the model clusters.

To better approximate the resulting cluster masses, we realize that cluster formation is a complicated dynamical process and the initial mass of the cluster-forming sphere does not reflect the evolving accretion rate due to feedback. In order to include this effect, we present a simple cluster formation model by assuming a decreasing mass accumulation history that is derived from Section 3.5: $\dot{M}(t) = \dot{M}_0(t/t_0)^{-1/2}$, where t_0 is the timescale that a cluster maintains the initial growth rate before the rate starts to decrease and $\dot{M}_0 = \epsilon_{\text{ff}} M_{\text{sp}} / \tau_{\text{ff}}$ is the initial cluster formation rate in a sphere with molecular mass M_{sp} . Therefore, the projected cluster mass is:

$$M = \int_0^{t_{\text{max}}} \dot{M}(t) dt = \frac{16\epsilon_{\text{ff}}}{\pi} \sqrt{\frac{G t_0 t_{\text{max}}}{D_{\text{GMC}}^3}} M_{\text{sp}}^{3/2} \quad (16)$$

assuming a constant density within the sphere of diameter D_{GMC} .

We rescale the sphere mass function using Eq. (16), and find that the slope of the expected cluster mass function is very similar to that of the CIMF. Also the maximum projected cluster mass can reach as high as $10^7 M_{\odot}$, similar to the max-

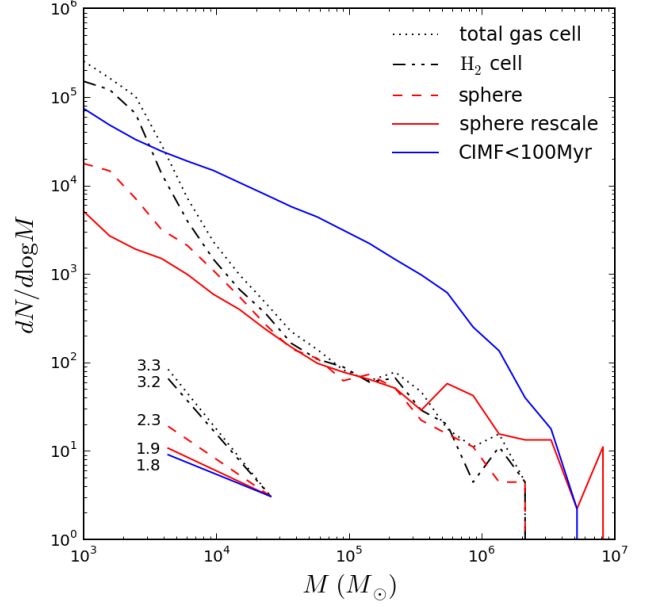


Figure 12. Mass functions of the simulation cells (black), cluster-forming spheres (red), and star clusters (blue) within the virial radius of the main galaxy at $z \approx 3.3$. Dotted and dashed dotted black lines show the distribution of total and molecular gas mass in simulation cells that are rescaled to the volume of the cluster formation sphere. Red dashed line is the mass function of molecular gas within cluster formation spheres. Red solid line presents the distribution of projected cluster masses that is estimated by a simple accretion model with given sphere masses, see text in details. The best-fit slopes of all mass functions are shown in the lower left corner with line styles the same as the main plot.

imum cluster mass. This consistency indicates that the origin of CIMF is the combination of the decreasing mass growth history and the mass function of the molecular gas in the cluster-forming regions.

In the expected cluster mass function, the power-law shape extends to very high mass and there exists no clear high mass cutoff as seen in the CIMF. This may be caused by very strong feedback from the most massive cluster particles. We estimate the expected mass using Eq. (16) by assuming all clusters follow the same mass growth history: $\dot{M} \propto t^{-1/2}$. This simple analytical expression may miss a mass-dependent factor that reflects the variability of clusters with different masses. Indeed, more massive clusters usually have stronger feedback, so that their growth can be terminated earlier than the less massive ones.

4.3. On the high mass end of CIMF

Although various observations of young massive clusters in nearby galaxies suggest a power-law mass function, it is still debated whether there exists a high mass cutoff in the CIMF and whether the cutoff mass is environment-dependent. Larsen (2002) found a correlation between SFR and the V-band magnitude of the brightest clusters and suggested that cluster formation is a stochastic process and the maximum luminosity of the clusters can be explained by statistical sampling from a universal CIMF, so-called “size-of-the-sample” effect. Other observations in various environ-

ments suggest that the variation of the high mass end of the CIMF may reflect different physical condition of their host galaxies (Bastian 2008; Goddard et al. 2010; Adamo et al. 2015). More recently, Sun et al. (2016) analyzed the cluster mass-galactocentric distance relation in four galaxies and concluded that, at least statistically, it is hard to rule out the environment-independent cluster formation scenario.

In our simulations, we have a large number of young cluster samples that are formed at different epochs in different galaxies. Therefore, we can study the influence of environment on the model CIMF. First, we find a strong correlation between the fraction of clustered star formation Γ and the SFR surface density Σ_{SFR} , shown in Figure 9. If the shape of the CIMF does not change with environment and the most massive clusters are formed merely due to the “size-of-the-sample” effect, Γ will be constant for different SFR and have larger scatter for lower SFR cases. However, the apparent positive correlation between Γ and Σ_{SFR} suggests that massive clusters are preferentially formed in starbursts. This in turn implies an environment-dependent cluster formation process and disfavors the stochastic scenario. Second, direct fit of the CIMF suggests a positive correlation between the cutoff mass M_{cut} and SFR of the host galaxy. This directly supports the environmental-dependent CIMF. The maximum cluster mass would be strongly overestimated by assuming a pure power-law CIMF, but it is in agreement with the predicted value when assuming a Schechter function with M_{cut} that is inferred from the empirical M_{cut} -SFR relation. All these results validate a Schechter CIMF with a environment-dependent cutoff mass in our model.

4.4. On the origin of globular clusters

Massive star clusters, especially those with mass $\gtrsim 2.6 \times 10^5 M_{\odot}$, have lifetime comparable to the age of the Universe (Muratov & Gnedin 2010). Therefore, they can be considered as progenitors of present-day globular clusters (GCs). Studying the formation of young massive clusters at high red-shift gives us an opportunity to investigate the origin of GC populations. Ashman & Zepf (1992) proposed a model of GC formation in the gas-rich major mergers. Recently, Muratov & Gnedin (2010) and Li & Gnedin (2014) incorporated this scenario in semi-analytical models to study the GC properties in the Milky Way and the Virgo galaxies, and successfully reproduced the multi-modal metallicity distribution of GCs.

Following the idea that cluster formation is a strong environment-dependent process, there are two requirements for the formation of massive clusters. First, the CIMF needs to have a high cutoff mass so that the probability of sampling massive clusters is not too low. For instance, in order to obtain $M_{\text{cut}} = 10^6 M_{\odot}$, the corresponding SFR needs to reach as high as $14 M_{\odot}/\text{yr}$ based on Eq. (7). The SFR of this level is hard to achieve during the quiescent evolutionary stage of a Milky Way-sized galaxy at high red-shift, but can be reached when the galaxy experiences major mergers. Second, to form such massive clusters, the host galaxy needs to have a large amount of cold gas so that the formation of most massive clusters is not limited by the “size-of-the-sample” effect. Indeed, as we can see from Section 3.3, massive clusters in our simulations are preferentially formed during the gas-rich major merger epochs.

Another possible dynamical effect of major mergers on the GC formation is that, major merger kicks massive clusters out of their birthplace in the galactic disk with high gas and stellar density, and places them into the stellar halo where the tidal

field is weak. This process helps to protect the newly formed clusters from being quickly destroyed by the intense tidal field in the disk. This two-stage formation and evolution scenario (Kruijssen 2015) can also be tested in our model by analyzing the bound fraction evolution, as discussed in Section 2.2. This dynamical migration process will help us understand the transition from young massive clusters at high red-shift to the GCs that we observe in the local Universe.

5. SUMMARY

In this paper, we introduced a new star formation implementation, in which star cluster is considered as a unit of star formation and cluster particle accumulates mass from a fixed sphere with size similar to the observed half-light radii of massive clusters. The mass growth of a given cluster particle is terminated by its own feedback, so that its final mass is obtained self-consistently and represents well the mass of a newly formed star cluster in the cluster-forming region. We implemented this CCF model in the ART code, and performed several high resolution cosmological simulations of the Milky Way-sized galaxy under different model parameters. The main results are summarized below.

- The CIMF in both the main and satellite galaxies is best described by a Schechter function, with a power-law slope $\alpha \sim 1.8$, similar to the observed young massive clusters in nearby galaxies. The shape of the CIMF is not sensitive to the model parameters, except for model SFE100. The CIMF of SFE100, with 100% star formation efficiency per free-fall time, has a cutoff mass that is much smaller than other models and is inconsistent with observations.
- We find a positive correlation between the SFR and the cutoff mass M_{cut} . The maximum cluster mass is consistent with the theoretical estimation by assuming a Schechter-like CIMF. We also find a tight correlation between SFR surface density and fraction of clustered star formation. Galaxies with stronger star formation activity are more likely to create larger fraction of massive clusters. Both evidences suggest that cluster formation is a local process that strongly depends on environment. The scenario that clusters are formed by stochastic sampling from a universal CIMF is ruled out.
- The mass accumulation history of different cluster particles is roughly described by a decreasing mass growth rate, $\dot{M} \propto t^{-1/2}$, with large scatter. The mass-weighted cluster formation timescale is within 4 Myr, consistent with the age spread of observed young star clusters. Both the decreasing mass growth history and the short cluster formation timescale indicate that cluster formation is strongly influenced by their own feedback. The power-law slope of the CIMF arises from a combination of the decreasing mass growth history and the mass function of the molecular gas in the cluster-forming regions, rather than that of the gas cells, indicating the necessity of the mass accumulation from the fixed-size region within which cells with various densities are enclosed.
- We analyze the time series of both the formation rate of massive clusters and the merger ratio of the main halo, and find that the formation of massive clusters synchronizes well with the major merger events???. By

realizing these massive clusters can be considered as the progenitors of the GCs that are observed at present, our model supports the scenario that GCs are preferentially formed during gas-rich major mergers. This in

turn suggests that the current GC populations contain fossil record of the merger history of their host galaxies.

REFERENCES

- Adamo, A., Kruijssen, J. M. D., Bastian, N., Silva-Villa, E., & Ryon, J. 2015, *MNRAS*, 452, 246
- Agertz, O., & Kravtsov, A. V. 2015, *ApJ*, 804, 18
- Agertz, O., Kravtsov, A. V., Leitner, S. N., & Gnedin, N. Y. 2013, *ApJ*, 770, 25
- Aravena, M., Spilker, J. S., Bethermin, M., et al. 2016, *MNRAS*, 457, 4406
- Ashman, K. M., & Zepf, S. E. 1992, *ApJ*, 384, 50
- Bastian, N. 2008, *MNRAS*, 390, 759
- Bate, M. R., Bonnell, I. A., & Price, N. M. 1995, *MNRAS*, 277, 362
- Behroozi, P. S., Wechsler, R. H., & Conroy, C. 2013a, *ApJ*, 770, 57
- Behroozi, P. S., Wechsler, R. H., & Wu, H.-Y. 2013b, *ApJ*, 762, 109
- Behroozi, P. S., Wechsler, R. H., Wu, H.-Y., et al. 2013c, *ApJ*, 763, 18
- Bigiel, F., Leroy, A., Walter, F., et al. 2008, *AJ*, 136, 2846
- Cen, R., & Ostriker, J. P. 1992, *ApJL*, 399, L113
- Ceverino, D., Klypin, A., Klimek, E. S., et al. 2014, *MNRAS*, 442, 1545
- Federrath, C., Banerjee, R., Clark, P. C., & Klessen, R. S. 2010, *ApJ*, 713, 269
- Genzel, R., Tacconi, L. J., Lutz, D., et al. 2015, *ApJ*, 800, 20
- Gieles, M., Larsen, S. S., Bastian, N., & Stein, I. T. 2006, *A&A*, 450, 129
- Gnedin, N. Y. 2014, *ApJ*, 793, 29
- . 2016, *ArXiv e-prints*, arXiv:1603.07729
- Gnedin, N. Y., & Abel, T. 2001, *New A*, 6, 437
- Gnedin, N. Y., & Kravtsov, A. V. 2011, *ApJ*, 728, 88
- Gnedin, N. Y., Kravtsov, A. V., & Rudd, D. H. 2011, *ApJS*, 194, 46
- Gnedin, O. Y., Ostriker, J. P., & Tremaine, S. 2014, *ApJ*, 785, 71
- Goddard, Q. E., Bastian, N., & Kennicutt, R. C. 2010, *MNRAS*, 405, 857
- Governato, F., Zolotov, A., Pontzen, A., et al. 2012, *MNRAS*, 422, 1231
- Haardt, F., & Madau, P. 2001, in *Clusters of Galaxies and the High Redshift Universe Observed in X-rays*, ed. D. M. Neumann & J. T. V. Tran
- Hartmann, L., Ballesteros-Paredes, J., & Heitsch, F. 2012, *MNRAS*, 420, 1457
- Hopkins, P. F., Kereš, D., Oñorbe, J., et al. 2014, *MNRAS*, 445, 581
- Hummels, C. B., & Bryan, G. L. 2012, *ApJ*, 749, 140
- Katz, N. 1992, *ApJ*, 391, 502
- Keller, B. W., Wadsley, J., & Couchman, H. M. P. 2015, *MNRAS*, 453, 3499
- Kravtsov, A. V. 1999, PhD thesis, NEW MEXICO STATE UNIVERSITY
- . 2003, *ApJL*, 590, L1
- Kravtsov, A. V., Klypin, A. A., & Khokhlov, A. M. 1997, *ApJS*, 111, 73
- Kroupa, P. 2001, *MNRAS*, 322, 231
- Kruijssen, J. M. D. 2012, *MNRAS*, 426, 3008
- . 2014, *Classical and Quantum Gravity*, 31, 244006
- . 2015, *MNRAS*, 454, 1658
- Krumholz, M. R., Dekel, A., & McKee, C. F. 2012, *ApJ*, 745, 69
- Krumholz, M. R., McKee, C. F., & Klein, R. I. 2004, in *Astronomical Society of the Pacific Conference Series*, Vol. 323, *Star Formation in the Interstellar Medium: In Honor of David Hollenbach*, ed. D. Johnstone, F. C. Adams, D. N. C. Lin, D. A. Neufeld, & E. C. Ostriker, 401
- Lada, C. J., & Lada, E. A. 2003, *ARA&A*, 41, 57
- Larsen, S. S. 2002, *AJ*, 124, 1393
- Larson, R. B. 1981, *MNRAS*, 194, 809
- Li, H., & Gnedin, O. Y. 2014, *ApJ*, 796, 10
- Mac Low, M.-M., & Klessen, R. S. 2004, *Reviews of Modern Physics*, 76, 125
- McKee, C. F., & Ostriker, E. C. 2007, *ARA&A*, 45, 565
- Munshi, F., Governato, F., Brooks, A. M., et al. 2013, *ApJ*, 766, 56
- Muratov, A. L., & Gnedin, O. Y. 2010, *ApJ*, 718, 1266
- Navarro, J. F., & White, S. D. M. 1993, *MNRAS*, 265, 271
- Padoan, P., Haugbølle, T., & Nordlund, Å. 2012, *ApJL*, 759, L27
- Planck Collaboration, Ade, P. A. R., Aghanim, N., et al. 2014, *A&A*, 571, A15
- . 2015, *ArXiv e-prints*, arXiv:1502.01589
- Portegies Zwart, S. F., McMillan, S. L. W., & Gieles, M. 2010, *ARA&A*, 48, 431
- Read, J. I., Agertz, O., & Collins, M. L. M. 2015, *ArXiv e-prints*, arXiv:1508.04143
- Renaud, F., Bournaud, F., & Duc, P.-A. 2015, *MNRAS*, 446, 2038
- Rudd, D. H., Zentner, A. R., & Kravtsov, A. V. 2008, *ApJ*, 672, 19
- Saintonge, A., Lutz, D., Genzel, R., et al. 2013, *ApJ*, 778, 2
- Salem, M., & Bryan, G. L. 2014, *MNRAS*, 437, 3312
- Scannapieco, C., Tissera, P. B., White, S. D. M., & Springel, V. 2006, *MNRAS*, 371, 1125
- Scannapieco, C., Wadehuhl, M., Parry, O. H., et al. 2012, *MNRAS*, 423, 1726
- Scudder, J. M., Ellison, S. L., Torrey, P., Patton, D. R., & Mendel, J. T. 2012, *MNRAS*, 426, 549
- Semenov, V. A., Kravtsov, A. V., & Gnedin, N. Y. 2015, *ArXiv e-prints*, arXiv:1512.03101
- Springel, V., Frenk, C. S., & White, S. D. M. 2006, *Nature*, 440, 1137
- Stinson, G., Seth, A., Katz, N., et al. 2006, *MNRAS*, 373, 1074
- Sun, W., de Grijs, R., Fan, Z., & Cameron, E. 2016, *ApJ*, 816, 9
- Tacconi, L. J., Neri, R., Genzel, R., et al. 2013, *ApJ*, 768, 74
- Urquhart, J. S., Moore, T. J. T., Csengeri, T., et al. 2014, *MNRAS*, 443, 1555
- Vikhlinin, A., Kravtsov, A. V., Burenin, R. A., et al. 2009, *ApJ*, 692, 1060
- Wetzel, A. R., Hopkins, P. F., Kim, J.-h., et al. 2016, *ArXiv e-prints*, arXiv:1602.05957